Review

Recent Advances in C-Band High-Power and High-Speed Radio Frequency Photodiodes: Review, Theory and Applications

Saeed Haydhah , Fabien Ferrero , Xiupu Zhang * , Ahmed A. Kishk

Posted Date: 5 May 2025

doi: 10.20944/preprints202504.2204.v2

Keywords: Ge-on-Si photodiode; High-Power and High-Speed Photodiode; Silicon Photonics; C-band optical signal; radio-over-fiber; wireless 5G communication; mmWave antenna

doi:10.20944/preprints202504.2204.v2

Review

Recent Advances in C-Band High-Power and High-Speed Radio Frequency Photodiodes: Review, Theory and Applications

Saeed Haydhah [1], Fabien Ferrero [2], Xiupu Zhang [1*], and Ahmed Kishk [1]

[1] Department of Electrical and Computer Engineering, Concordia University, Montréal, QC H3G 1M8, Canada
[2] The Universit'e Cote d'Azur, CNRS, LEAT, Sophia Antipolis, 06410 France
* Correspondence: johnxiupu.zhang@concordia.ca

Abstract: A review of the recent research work on High-Power and High-Speed (HPHS) Ge-on-Si photodiodes design is presented, using Silicon Photonics (SiPh) technology, suitable for Radio-over-Fiber scheme. The Photodiode (PD) principle of operation, its structure for high RF photogenerated power, and the achieved wide bandwidth are presented. Followed by the PD equivalent circuit models which are introduced such that it is allowed to obtain the PD S-parameters and bandwidth. Then, the PD theoretical transit-time and RC-time bandwidths are presented, and the PD photocurrent behavior against input optical power and the optical signal manipulation techniques to improve the PD performance are also presented. After that, the impedance matching techniques between the PD output impedance and antenna input impedance are presented. Finally, the recent photonic mmWave antenna designs are introduced.

Keywords: Ge-on-Si photodiode; High-Power and High-Speed Photodiode; Silicon Photonics; C-band optical signal; radio-over-fiber; wireless 5G communications; mmWave antenna

1. Introduction

Global mobile traffic and the number of subscribers to the wireless network are increasing dramatically with time [1]. Therefore, the 5G network is the key solution for the wireless network to provide reliable connections for the incoming huge number of subscribers and applications. The communication data rates are increasing sharply [1]. Thus, fast optical counterparts are replacing the slow electrical components in communications systems, so that the data rates can be sharply increased. Thus, communication systems are developed into new schemes where electric Radio-Frequency (RF) components are directly interfaced with optical components. As shown in Figure 1, the conversion from the optical to electric domain is achieved using High-Power and High-Speed (HPHS) photodiodes. On the other hand, the conversion from the electric to the optical domain is obtained by modulating optical sources. Furthermore, these photodiodes and optical modulators are connected to microwave components such as antennas or electric amplifiers [2]. The photodiodes for wireless communication applications must operate at high speeds for higher communication data rates and high RF photogenerated powers for enhanced Signal-to-Noise Ratios (SNR) and signal coverage range.

The HPHS photodiodes can be designed using the III-V semiconductor material or achieved using the Silicon Photonics (SiPh) technology. The III-V photodiodes have been reported to achieve high output RF powers with wide operating bandwidths. However, the III-V photodiodes are very complex to be integrated with the Complementary Metal-Oxide Semiconductor (CMOS) technology, making them complex to be integrated with electronics. On the other hand, the Germanium-on-Silicon (Ge-on-Si) photodiodes implemented using the SiPh technology can easily be integrated with the CMOS technology. However, the reported Ge-on-Si photodiodes did not achieve as high powers as the RF powers achieved by III-V photodiodes, and they also did not achieve as wide bandwidths as the bandwidths achieved by III-V photodiodes.

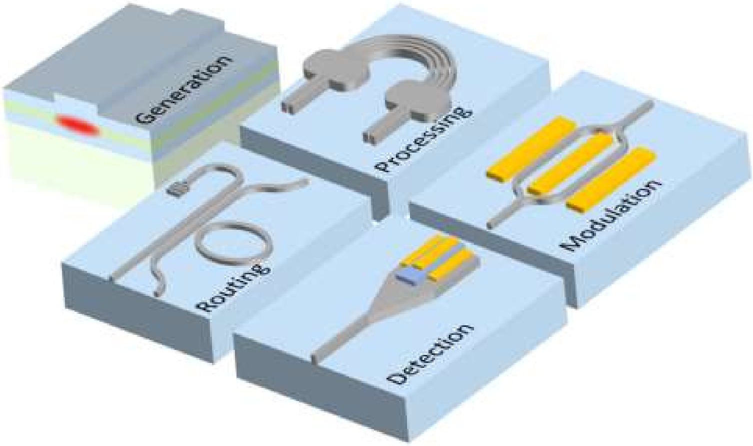

Figure 1. Photonic integrated circuits include photonic light generation, photonic signal processing, photonic signal routing, optical light detection, and optical modulation [3].

In addition, microwave photonics circuits are much easier to be fabricated using the SiPh platform. On the other hand, if the photodiode is to be designed using the III-V semiconductor material, fabricating it is a complex and high-cost task. Thus, it leads to a complicated integration process with SiPh or CMOS systems. The Silicon Photonics technology applies the CMOS processing techniques to obtain photonic, opto-electronic, and microwave photonics circuits [3]. On a SiPh chip, many different optical and electrical components can be installed and interfaced, such as Light-Emitting-Diodes, optical waveguides, optical signal processing components, photodiodes, optical modulators, antennas, mmWave circuits and so on [3]. Therefore, the SiPh platform provides an important opportunity for the optical and microwave components to be integrated on the same substrate, improving the data rates for the 5G technology and beyond.

This review article presents the recent developments in High-Power and High-Speed photodiodes used for Radio-over-Fiber (RoF) 5G wireless technology. This article is arranged as follows: Section 2 presents a recent review study for HPHS photodiodes, Section 3 presents important applications for microwave photonics circuits using HPHS photodiodes, and Section 4 concludes the paper.

2. High-Power and High-Speed RF Photodiodes

It has been reported that the photodiodes designed using the III-V semiconductor material on an Indium Phosphide (InP) substrate can provide high output RF powers that can sufficiently cover required wireless ranges for 5G base-stations radiations at mmwave frequencies [4]. The RF photogenerated power of III-V photodiodes reaches 25 dBm at 25 GHz, and 15 dBm at 65 GHz [4]. However, the III-V photodiodes are complex and high-cost to be fabricated, and they are challenging to integrate with CMOS and SiPh technology. On the other hand, the Ge-on-Si photodiodes, designed using SiPh technology, could provide sufficient output RF photogenerated powers at mmwave frequencies. Many High-Power and High-Speed (HPHS) Ge-on-Si photodiodes have been recently reported to be implemented for microwave photonics applications [5–26]. HPHS Ge-on-Si photodiodes can be achieved when the Ge absorbing region is optically fed using evanescent coupling with double lateral Silicon Nitride waveguides [5]. They can also be obtained using a mode-evolution-based coupler, illuminating the light into the Ge region uniformly to reduce the saturation effects at high input optical powers [6–7]. In addition, they can be achieved when many photodiodes are connected in parallel to form a photodiode linear array [8–14]. Also, when the photodiode doping concentrations are regulated, the space-charge screening effects sharply decrease [15]. In addition, HPHS photodiodes (PDs) can be achieved when it is constructed using stacking N-, intrinsic- and P-type doped regions, and the light is evanescently coupled into the Ge region [16–17]. Furthermore, HPHS PDs can be achieved using the Uni-Traveling Carrier (UTC) approach, where the electrons are the only allowed carriers, and the slow holes are blocked and excluded [18]. UTC PDs can also be achieved using the III-V material, which are then integrated heterogeneously on the Silicon (Si) substrate [19]. The avalanche gain can also provide HPHS Ge-on-Si PDs [20–23]. However, most Avalanche PDs are designed for data communications applications at the O-band. Traveling-wave photodiodes can also achieve HPHS PDs [24–25]. It was also found that when the optical field is manipulated properly around the Ge absorbing region, higher output RF powers are expected to be obtained from the PDs [26]. Table 1 presents the performance comparison between the introduced Ge-on-Si PDs.

It is worth mentioning that Germanium is a good medium for absorbing optical signals with wavelengths just before 1600 nm [27]. The absorption coefficients of the Ge medium are $10^4\ cm^{-1}$ at $1310\ nm$, and $5 \times 10^3\ cm^{-1}$ at $1550\ nm$. Therefore, the Ge material is a perfect option to be used as the absorbing medium for photodiodes which are used for data centers at 1300 nm, and it is also a good option for the photodiodes which can be used for 5G base stations at 1550 nm. However, InGaAs material is more efficient at 1550 nm wavelength; however, Ge is used for PD design as it is much easier to integrate within a Silicon chip using the SiPh platform.

2.1. Photodiode Principle and Structures

When the light is evanescently coupled from double lateral waveguides to the Ge region, the PD is expected to provide high-power and high-speed operation [5]. The evanescently coupled PD is shown in Figure 2. The light distribution in the absorption Ge region is uniform due to the tapering of the lateral waveguides. As a result, the photogenerated carriers are not concentrated at a specific location, and the operating bandwidth of the PD is increased. In addition, the applied electrostatic field between the PD electrodes is also sufficiently strong due to the doping concentrations used for the N+-, P-, and P+-region. Therefore, the collection of the photogenerated carriers is fast and efficient. The lateral waveguides are sufficiently long, so the injected photons are fully absorbed as they travel along the Ge region. Phase matching between the waveguide and Ge region modes should be achieved to obtain efficient light coupling [28]. Many parameters affect the mode coupling condition, such as the waveguide thickness, the Ge region thickness, the refractive indices of the waveguide and Ge region, and the operating wavelength.

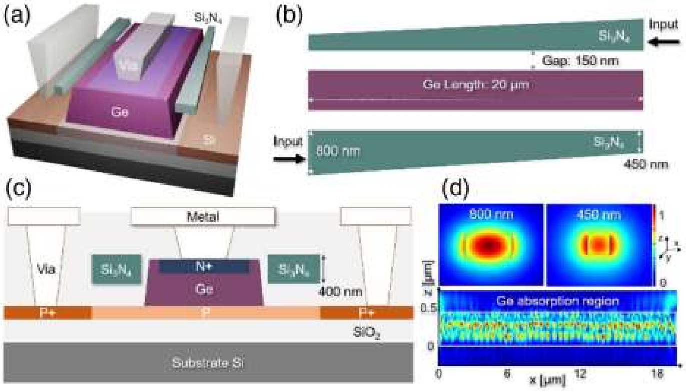

Figure 2. The Ge-on-Si photodiode using double lateral Si_3N_4 optical waveguides [5]. (a) Side view of the photodiode, (b) Top view of the PD, (c) Cross-sectional view of the PD, and (d) Electric field distribution across the Si_3N_4 waveguides, and along the Ge absorbing medium.

When the photodiode is operated under high-power conditions, that is, when the input optical power is 10 mW or more, then the photodiode suffers from degraded linearity, heat failure occurrence, losing the mode matching between the waveguide and Ge region, and accumulation of charges causing the space-charge effects to take place. The mode-evolution-coupling technique can achieve HPHS PDs [6–7]. Figure 3 shows the proposed mode-evolution-based coupled HPHS PD in [7]. The optical light is divided into two optical waveguides using a Multimode Interferometer (MMI) power divider such that two parallel Ge regions are equally fed using the mode-evolution-based coupling technique. The mode-evolution-based coupler comprises the waveguide bend and the linearly tapered waveguides. The waveguide bend reduces the mode mismatch between the waveguide and the Ge region. Therefore, the bend radius should be as large as possible to achieve a gradual mode transition. The waveguide taper allows the light to couple into the Ge region gradually and efficiently; as a result, a uniformly distributed optical generation rate along the PD length is achieved, and the PD saturation current is improved. The waveguide taper length should be as long as possible to increase the PD responsivity; however, the PD bandwidth will be reduced due to increased capacitance. It is worth noting that when the Ge region was divided into two halves, the input optical power at each Ge region was reduced by half, the space-charge effects were much reduced, and the saturation current was much improved. The proposed HPHS PD in [7] achieved a dark current of 73 nA at -1 reverse bias, and a photocurrent of 9.4 mA at an input optical power of 20 mW. The high-power operating bandwidth of the PD is 31.6 GHz when the input optical power is 4 mW.

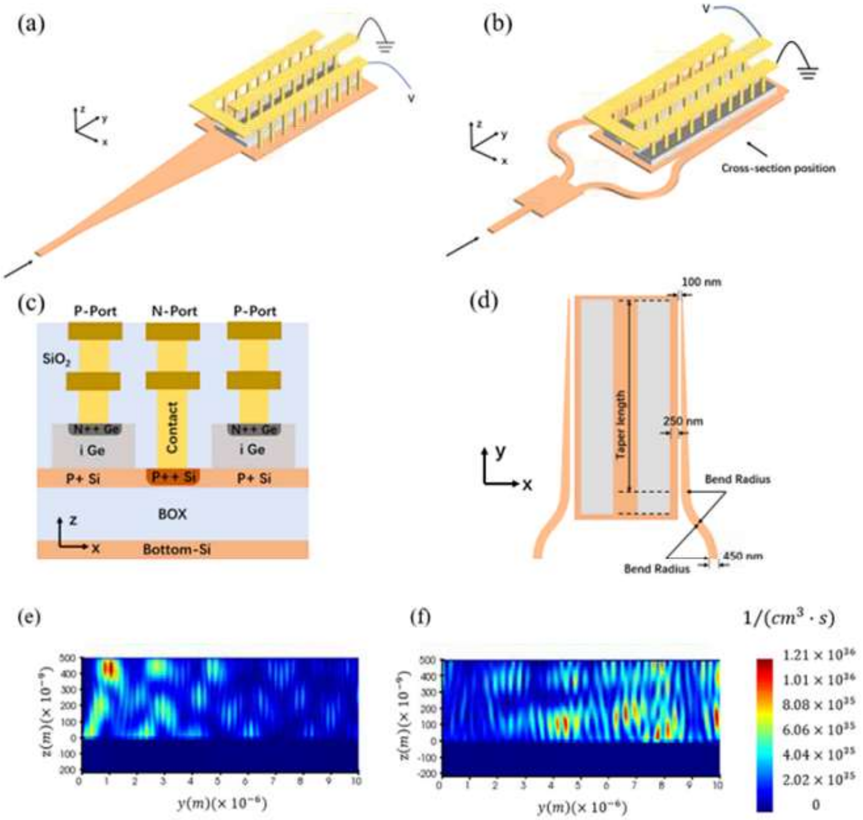

Figure 3. (a) Butt-coupled PD with 50 um long taper. (b) The proposed mode-evolution-based coupled PD [7]. (c) The cross-section view of the proposed PD. (d) The top view of the proposed PD. (e) The optical generation rate for the butt-coupled PD. (f) The optical generation rate for the proposed mode-evolution-based coupled PD.

Furthermore, the Ge regions can be connected in parallel using a single Ground-Signal-Ground (GSG) terminal to enhance the output power of the photodiode [8–14]. When two Ge regions are connected in parallel, the total Ge area is increased twice. As a result, the junction capacitance increases by a factor of two, and the series resistance decreases by a factor of two also; as a result, the PD RC-time bandwidth is not changed, and the PD saturation current is sharply increased. Hence, the PD output RF power is increased sharply as well. The array of two elements proposed in [8] is illuminated by light from the front and back sides of the Ge regions; as a result, the absorption rate along the Ge regions has a uniform distribution, causing the space-charge effects to be reduced sharply, and at the same time, the saturation current increases sharply. In addition, when the PD is illuminated by light from both sides, then the applied optical power on the Ge regions is reduced by a factor of 0.5, which decreases the chances of thermal failures sharply. The dark current of the PD array has increased compared to the dark current of the single-element PD.

When the number of elements of the PD array is increased to be more than two elements, then the PD array saturation current will be increased, but the PD array RC bandwidth will be changed from that of the single-element PD because the PDs resistances will not be connected in parallel. Therefore, the RC bandwidth of the PD array can be calculated using the transmission matrix method to analyze the resulting complicated PD equivalent circuit, as was proposed in [9], where all the Ge regions share the same P+ doped region. It was found that when more than two array elements are used, then the PD array bandwidth will be reduced as the junction capacitance increase will be the dominant affecting factor, and the array total resistance will not decrease. However, the bandwidth of the PD array can be enhanced using inductive peaking techniques and transmission line theory. The saturation current of the PD array with more than two array elements will gradually increase, because there will be high power losses in the P+ doped region resistances, and due to out-of-phase currents flowing in these resistances [9].

Traveling Wave PD Array (TWPDA) can also be designed to avoid bandwidth reduction by using more than two array elements [10]. The used single-element PD for the four-element TWPDA proposed in [10] is a PIN PD [16, 28 – 29] with a high photocurrent and a wide bandwidth. The impedance matching between the TWPDA and a 50 Ohm load is achieved by optimizing the GSG coplanar-waveguide electrodes connected to the four PD elements, considering the periodic capacitive PD loading. In addition, it can be seen from Figure 4, showing the proposed TWPDA in [10], that optical delay lines match the optical velocity with the electrical velocity. On the other hand, it can be seen from Figure 5, showing the proposed TWPDA in [11], that this proposed PD array has single-element PDs illuminated from the front and back sides such that the power handling capability of the PD array is doubled.

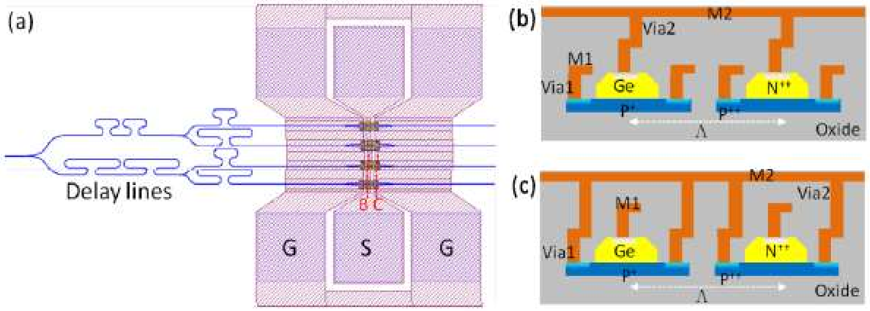

Figure 4. (a) The travelling-wave PD array in [10], (b) Signal metal connections to the single-element PDs at the B position, and (c) Ground metal connections to the single-element PDs at the C position.

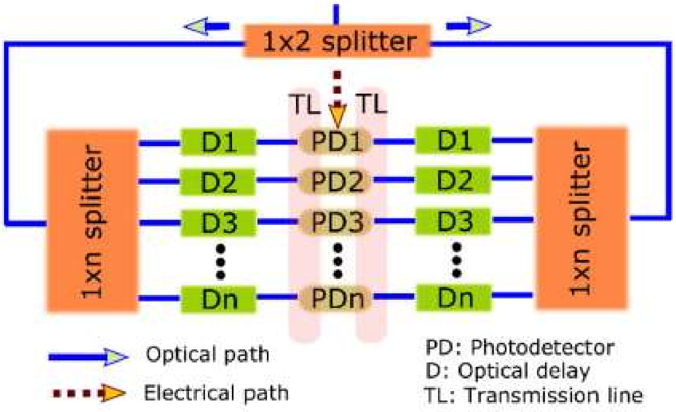

Figure 5. The High-Power and High-Speed dual-illuminated TWPDA in [11].

The traveling wave photodiode approach was also used to provide a High-power and High-Speed Photodiode as proposed in [24–25]. The traveling wave photodiodes are designed with metallic electrodes that achieve the impedance matching with an external circuit. The transmission line theory matches the impedance between the microstrip or coplanar waveguide electrode lines and the output circuit (50 Ohm load, for example). The input terminal of the electrodes will also be connected to a matched load such that the backward traveling waves are absorbed and not reflected in the transmission lines. Hence, the TWPD bandwidth is engineered using the transmission line theory, and the PD RC-time bandwidth, carrier drift time, carrier diffusion, carrier trapping, and the bandwidth of velocity matching between the electrical and optical signal will also impact it. It can be seen from Figure 6 that the proposed TWPD in [25] is optically dual-injected and evanescently coupled to the Ge region. The TWPD length is optimized to achieve the best PD performance when the uniform light distribution occurs in the Ge region because the left- and right-incoming optical signals will add up constructively to provide a uniform distribution. As a result, the effective absorption area is increased, and the saturation performance is much improved. The RC time constant, the carrier transit time, and the electrodes length limit the 3 dB bandwidth of this proposed TWPD. When the PD electrodes are longer, the PD capacitance and transmission line loss are increased; as a result, the PD bandwidth decreases. Also, when the PD length provides non-uniform light field distribution, the bandwidth will decrease because of increased space-charge screening effects. Also, the PD bandwidth decreases when the input optical power increases due to the increase in the space-charge screening effects and the much higher probability of carriers collisions with the lattice.

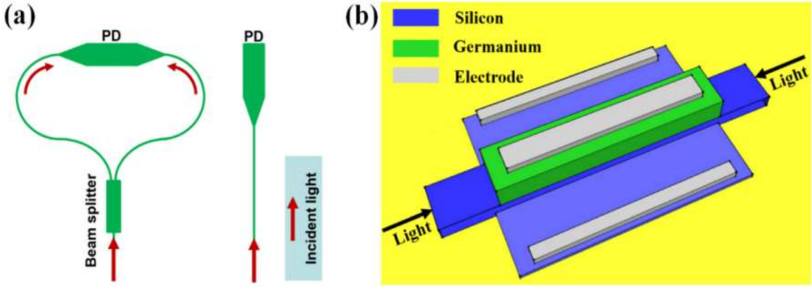

Figure 6. (a) Incident light is split into two beams to feed the PD, and (b) The proposed dual-injection PD in [25].

doi:10.20944/preprints202504.2204.v2

The HPHS PD can also be achieved when doping concentrations are regulated to reduce space-charge screening effects significantly [15]. The doping-regulated Ge-on-Si PD is shown in Figure 7, where it can be seen that the Ge region is sandwiched between the N++ doped region and P+ and P++ doped regions. When the doping concentration in the P+ collection layer is increased, the number of holes in the collection layer is much higher than the photogenerated carriers in the absorption Ge region, and the built-in electric field is much enhanced. As a result, the carriers' transport speed is much enhanced such that it achieves saturation velocity, the carriers' transit time is much reduced, the probability of carriers recombination is reduced, the photocurrent and saturation current are much increased, and the space-charge screening effects are eliminated.

In addition, when the optical signal is coupled evanescently to the Ge region of the PIN PD, then high-power at high speeds PDs can be achieved as they were reported in [16–17]. Also, Uni-Traveling Carrier (UTC) PD, where the only allowed carriers are the electrons, can be designed using the Ge-on-Si approach or using the heterogeneously integrated III-V material on Silicon (Si) to achieve HPHS PD performance [18–19].

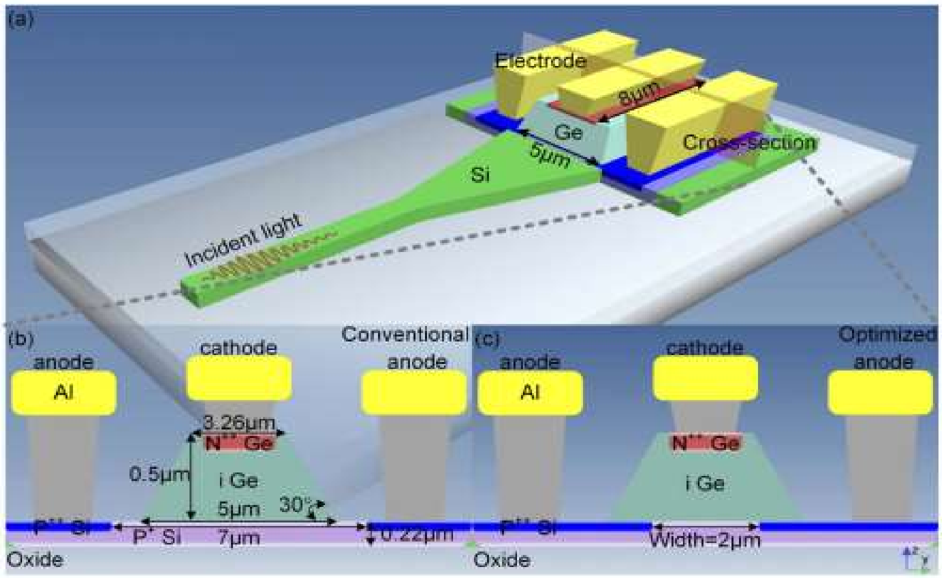

Figure 7. (a) 3D view of the doping-regulated PD in [15] and (b) PD with conventional doping regions. (c) The PD with the optimized doping regions.

Finally, the avalanche gain can increase the Ge-on-Si PD output power as proposed in [20–23]. However, these Avalanche Ge-on-Si PDs are reported to be used for data communications within data centers and not for 5G base stations with the RoF scheme. Hence, they are briefly presented here to show that using the Avalanche gain could introduce the opportunity of achieving HPHS PDs for 5G base station applications. The proposed Avalanche Photodiode (APD) is presented in Figure 8, which shows an example of an APD design. The proposed APD design achieves a bandwidth of 18.9 GHz, a DC photocurrent gain of 15, and a sensitivity of – 11.4 dBm at a reverse bias of – 6 V. It can be seen from Figure 8 that the APD has three terminals, and the Ge region is installed on top of the Si waveguide, and the waveguide is installed on top of a Si substrate. The optical signal is evanescently coupled to the Ge region for absorption. The top side of the Ge region is P-doped and connected to terminal one, while the Si substrate is composed of interdigitated N- and P-doped fingers spaced using intrinsic silicon. The P-doped fingers are connected to terminal two, and the N-doped fingers are connected to the third terminal. As a result, two reversed-biased PIN diodes are achieved, and the light absorption region is independently controlled from the charge multiplication region.

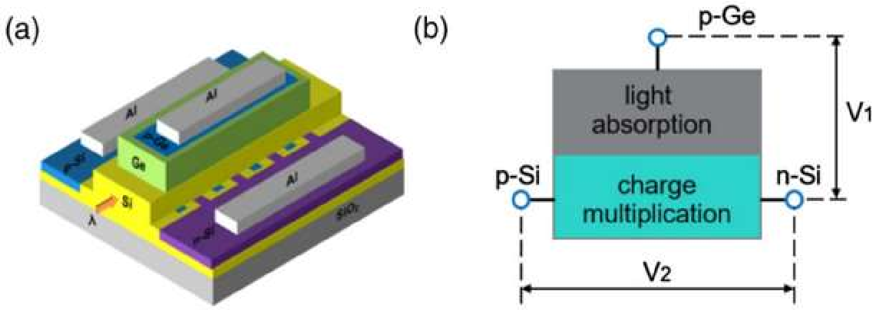

Figure 8. (a) The APD design in [23] and (b) Absorption and charge multiplication region.

Table 1. Comparison table between the introduced HPHS Ge-on-Si photodiodes in this article.

Photodiode	Res. (A/W)	HF Phc. (mA)	BW (GHz)	RF-P (dBm)	Dark Cur. (uA)	Appl.	DC Phc. (mA)
Ev. Coupled PD [5]	0.52	12	36	8.57	0.1	HP	16
Mode-Evolution PD [7]	0.47	1.88	31.6	-7.53	0.073	HP	9
2-Element PD [8]	0.46	13	9	9.27	1.28	HP	28.8
8-Element PD [9]	0.77	1	4.1	-13.01	3.46	HP	37
TWPD 4-Element [10]	0.82		20			HP	65
4-Element TWPDA [11]	0.76	13	35	9.26	>3.5	HP	112
TWPD [25]	1.07		11.4		0.0099	HP	13.28
8-Element PD [12]	0.21	48	5	14.3	15	HP	
4-Element PD [14]	0.58	19	15	7	0.3	HP	
Doping Regulated PD [15]	1.06	5.3	20	1.5	0.0014	HP	36.4
PIN PD [16]		40	4.38	14.17	125	HP	
Si-Based UTC PD [18]	0.5	2	30	-11.7	20	HP	
III-V UTC PD on Si [19]	0.95		40	12	0.01	HP	
Av. PD [20]	0.65		27	low	100	LP D-Com.	
Av. PD [21]			14	low		LP D-Com.	
Av. PD [23]			18.9	low		LP D-Com.	

Ev. ≡Evanescent, Av. ≡Avalanche, BW≡ Bandwidth, Res. ≡Responsivity, HF ≡High Frequency, Phc. ≡Photocurrent, RF-P≡ RF Power, Cur. ≡Current, Appl. ≡Applications, HP ≡High Power, LP ≡Low Power, D-Com. ≡Data Communications

doi:10.20944/preprints202504.2204.v2

2.2. Photodiode Equivalent Circuit Models

A fundamental equivalent circuit for a photodiode can be presented as shown in Figure 9 [5], where Cj represents the PD junction capacitance in the Ge absorption region, Cp represents the parasitic capacitance between the conductors of the Coplanar Waveguide (CPW) line, and Rs represents the series resistance of the highly P- and N-doped regions at the ohmic contacts on Silicon and Germanium. The junction capacitance C_j is a function of bias voltage and the Ge region geometry. While the series resistance R_s is a function of the doping concentrations at the ohmic contacts, and its value is usually around 50Ω when the PD area is small. It can be seen from Figure 9 that this PD equivalent circuit reveals the RC-time performance of the Ge-on-Si photodiode. In addition, many parameters were ignored in this equivalent circuit as their effects on the PD performance are negligible. Figure 10 [18] presents a more detailed equivalent circuit, where the CPW conductors are represented using the series inductance Lpad and the shunt capacitance Cpad. In addition, the junction resistance Rp is also included. This resistance R_p is usually very high because of the very small dark current, and it is usually safe to ignore this junction resistance.

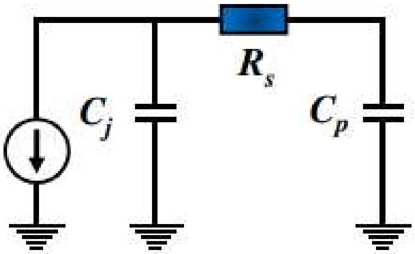

Figure 9. RC equivalent circuit for the Ge-on-Si PD in [5].

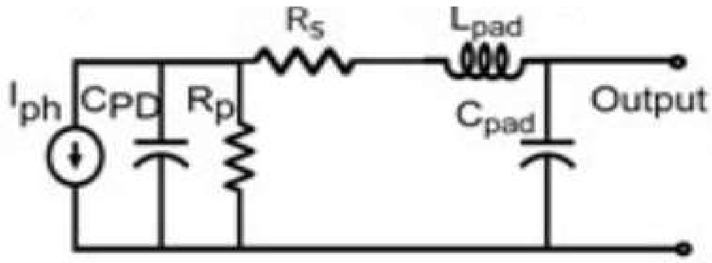

Figure 10. Equivalent circuit of the UTC PD in [18].

A more involved RF small-signal equivalent PD circuit is presented in Figure 11 [30], where the transit time and the RC time effects are included. It can be seen that the input voltage source $e_i(\omega)$ represents the input Radio-Frequency optical power component, followed by the PD transit-time equivalent circuit including R_t and C_t, where their values are optimized in the beginning so that the PD transit-time bandwidth is correctly achieved. The transit-time bandwidth is usually very high, with values that could reach around $200\ GHz$ or more, therefore, it can be ignored when the targeted operating frequencies are well below 100 GHz. The output voltage $e_o(\omega)$ represents the generated RF electric field in the PD absorption region, which drifts the free carriers to the PD external circuit. Therefore, the PD photocurrent is represented by the voltage-dependent current source $i(\omega)$, which is dependent on the generated RF electric field in the PD absorption region and the PD responsivity g_m. The PD photocurrent feeds the RC-time equivalent circuit and the PD load. The PD equivalent circuit in Figure 11 provides a more accurate frequency response for the photodiode. It is worth highlighting that the space-charge screening effects and thermal failure limit the output RF power from the photodiode. When the photodiode is operated under low-power conditions, the photodiode operates in its linear region since the electric field in the depletion region is not collapsed and free carriers drift with constant saturation velocity; as a result, the PD equivalent circuit is independent of the input optical power. On the other hand, the equivalent circuit is dependent on the input optical power when the photodiode is operated under high-power conditions because the PD transit-time and junction capacitance become dependent functions of the input optical power; as a result, the output RF power varies nonlinearly with the input optical power.

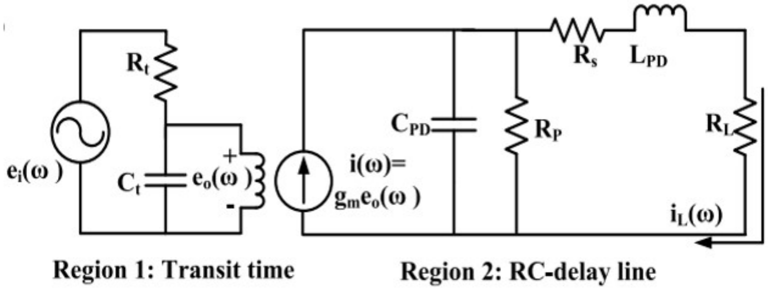

Figure 11. Photodiode equivalent circuit including the transit time and RC time effects [30].

It can be seen from Figure 12 and Figure 13 [31–32] that the PD equivalent circuit can also be designed including the CPW line model, where the S-parameters of the CPW line are included in the CPW line model in the equivalent circuit. It can be seen from Figure 13 that the PD CPW line is designed with an inductive-peaking transmission line tapered to a 50Ω line. Therefore, inductive peaking is achieved to enhance the photodiode bandwidth.

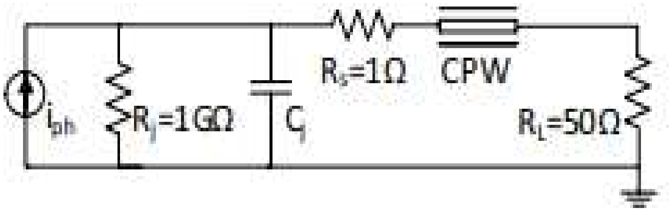

Figure 12. A more accurate PD equivalent circuit including the full-wave simulated PD CPW pads in [31].

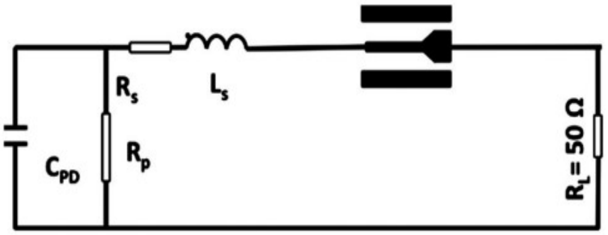

Figure 13. PD equivalent circuit including the simulated S-parameters of the PD CPW pads [32].

The equivalent circuit of the photodiode array, when it is composed of two elements, is presented in Figure 14 and Figure 15(b), [7–8]. It can be seen from Figure 14 and Figure 15(b) that the PD bandwidth is not decreased when two array elements are used because the two Ge regions are connected in parallel, and while the total junction capacitance is doubled, the total photodiode resistance is halved at the same time. As a result, the bandwidth of the PD array with two elements does not decrease when compared with the corresponding single-element PD bandwidth. This fact is obvious to obtain from Figure 15(b), where it can be seen that the junction capacitances of the two Ge regions and the element resistances are connected in parallel. The shunt topology in Figure 15(b) is chosen because the two Ge regions are connected in parallel as presented in Figure 14. It can be seen from Figure 14 that the PD element junction is available in the Ge region, and the top N++ Ge regions of the two elements are connected to the same ground electrode, while the P++ Si region of the two elements is connected to the same signal electrode. As a result, the two Ge regions are connected in parallel.

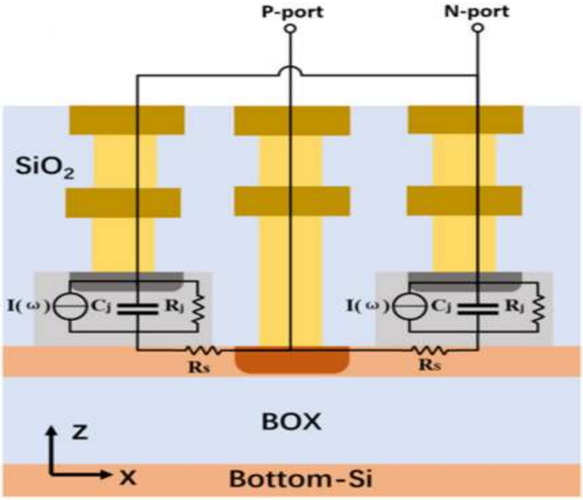

Figure 14. RC equivalent circuit for the PD array in [7].

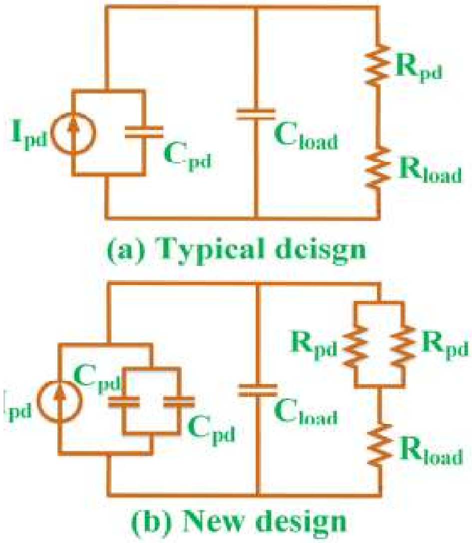

Figure 15. (a) Equivalent circuit for a single-element PD and (b) Equivalent circuit for a two-element PD array [8].

On the other hand, when the PD array is composed of more than two elements connected in parallel, as shown in Figure 16 [9], the bandwidth of the PD array is decreased. This is because the

doi:10.20944/preprints202504.2204.v2

elements' resistances and junction capacitances, R_{p_+} and C_j in Figure 16, are not connected in parallel, and this equivalent circuit should be analyzed using different mathematical approaches to find the PD array bandwidth; e.g., the transmission matrix method can be used to find the frequency response of the PD array with more than two elements. The power loss in the PD array with more than two elements will also increase. However, the overall saturation photocurrent increases sharply as the element numbers increase.

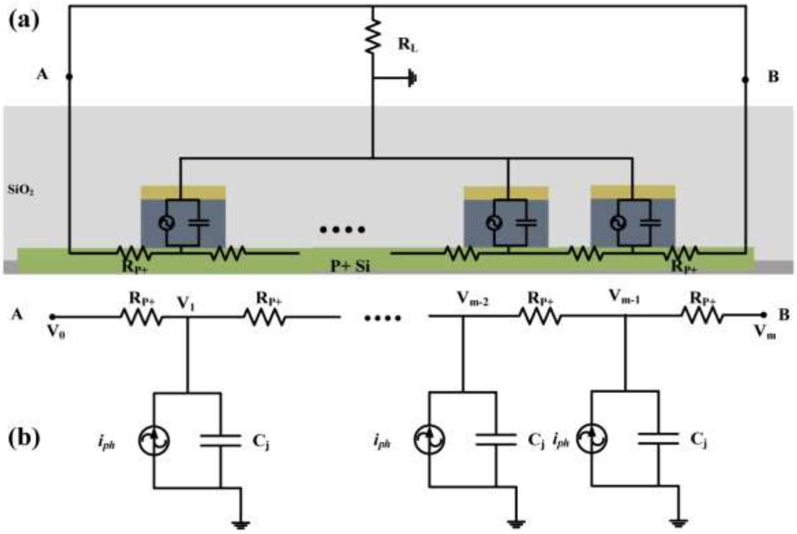

Figure 16. Equivalent circuit for the n-element PD array in [9].

2.3. Photodiode Bandwidth Design

The electrical 3 dB bandwidth of the photodiode is dominantly limited by the RC- time and transit-time bandwidths. The photodiode equivalent circuit can obtain the RC- and transit-time bandwidths. The carrier transit-time bandwidth for the Ge-on-Si PD in [5] was calculated as shown in Eq. (1)

$$f_{tr} = \frac{0.45 \times v_b}{d} \tag{1}$$

where v_b is the carrier drift velocity, and d is the thickness of the Ge region. The carrier drift velocity depends on the electric field strength; it is $v_b = 6 \times 10^6\ cm/s$ for the Ge medium [5]. The carrier transit-time can be defined as the required time for the photogenerated electrons and holes to travel from the absorption region to the collecting electrical electrodes. The holes' drift velocity dominantly limit the transit-time bandwidth for Ge-on-Si photodiodes because the holes are slower than electrons. On the other hand, the RC-time bandwidth was found to be calculated as shown in Eq. (2), [5] and [7]

$$f_{RC} = \frac{1}{2\pi R_{tot} C_{tot}} \tag{2}$$

where R_{tot} is the total PD resistance including the PD series ohmic-contact resistance, junction resistance, and load resistance, and C_{tot} is the total PD capacitance including the junction and parasitic capacitances. If the load resistance is set to zero, then the R_{tot} resistance can be found as shown in Eq. (3) [5]

doi:10.20944/preprints202504.2204.v2

$$R_{tot} = \frac{R_j R_s}{R_j + R_s} \tag{3}$$

where R_j is the PD junction resistance, and R_s is the series contact resistance. The junction capacitance can be found as shown in Eq. (4)

$$C_j = \frac{\varepsilon_o \varepsilon_r A}{d} \tag{4}$$

where ϵ_r is the dielectric constant of the Ge medium, A is the PD active area, and d is the depletion region depth.

The overall electrical 3 dB bandwidth can be obtained as shown in Eq. (5) [5].

$$f_{3\ dB} = \frac{1}{\sqrt{\frac{1}{f_{RC}^2} + \frac{1}{f_{tr}^2}}} \tag{5}$$

The RC-time bandwidth dominantly determines the electrical 3 dB low-pass bandwidth of the photodiode if the Ge thickness is small and the frequency of operation is not too high. It is worth highlighting the trade-off between the transit- and RC-time bandwidths. When the Ge thickness is decreased to improve the transit-time bandwidth, the RC-time bandwidth is degraded, and vice versa. In addition, the photodiode bandwidth, saturation RF power, and PD linearity are dependent parameters on the bias voltage and input optical power. The junction capacitance varies when the bias voltage changes because the PD depletion region width varies. As a result, the RC-time bandwidth is varied. On the other hand, when the input optical power increases, the space-charge screening effects increase, and the electric field in the absorption region decreases; as a result, the carrier velocity decreases and the transit-time bandwidth decreases.

The RC bandwidth of the PD array of two elements is equal to the RC bandwidth of the single-element PD. This part proves this concept mathematically. The RC-time bandwidth of the single-element PD can be written as shown in Eq. (6) [8].

$$f_{RC} = \frac{1}{2\pi(R_{pd} + R_{load})(C_{pd} + C_{load})} \tag{6}$$

And the RC-time bandwidth of the two-element PD array is shown in Eq. (7) [8].

$$f_{RC} = \frac{1}{2\pi\left(0.5R_{pd} + R_{load}\right)(2C_{pd} + C_{load})} \tag{7}$$

It can be seen from Eq. (6) and Eq. (7) that the total resistance of the PD array is divided by 2, and its total capacitance is multiplied by 2 because the two Ge regions are connected in parallel. Therefore, it can be seen from Eq. (6) and Eq. (7) that the RC bandwidth of the two-element PD array is almost equal to the RC bandwidth of the single-element PD. However, when the number of array elements is more than two, PD array bandwidth decreases as the number of elements increases.

2.4. Photodiode Saturation Current and RF Power

The photocurrent versus optical power characteristics of this proposed PD in [25] show that three photodiode operation regions can be deduced, as shown in Figure 17. The first operation region is obtained where the photocurrent is linearly increased versus the input optical power because the Ge region is not saturated yet. The second operation region is obtained where the photocurrent increases linearly with the input optical power but with a different slope. The Ge region in this operation region is partially saturated, and the saturated PD volume increases with the increase in input optical power. The third operation region is the saturation region where the carriers in the Ge region are fully saturated; the carriers inside the light field distribution are fully saturated, and as a result, the photocurrent does not increase when the optical power increases.

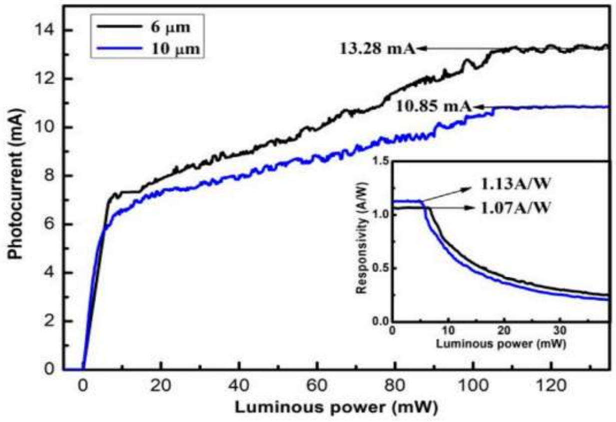

Figure 17. Photocurrent versus optical power characteristics for the proposed PD in [25].

In general, the output RF photogenerated power can be found in dBm using Eq. (8). In addition, the saturation current which starts in the nonlinear operation region can be defined as the average photocurrent at which the RF power compressions curve drops by $1\ dB$ from its peak value.

$$P_{RF} = 10 \times \log\left(\frac{0.5 \times R_L \times I_{ph}^2}{1 \times 10^{-3}}\right) \quad [dBm] \tag{8}$$

It is worth noting that the PD power handling capability and saturation performance can be much improved when the incident light field is illuminated on the double sides of the Ge absorption region using different optimized manipulation approaches to allow the absorption profile to spread more uniformly across the PD absorption region. Different light manipulation approaches are proposed in [26], as shown in Figure 18. Type B PD has three sections where Section 1 is used to generate multi-modes, and the light is manipulated to provide a good pattern before reaching the Ge region. Section 2 allows the light to be illuminated in the front and side parts, which results in an optimized light distribution and a new absorption profile in the Ge region. Section 3 is designed so that the light is fully absorbed. Type B PD is modified to be double-sided illuminated using a 1×2 MMI (MultiMode Interferometer) splitter shown as type C PD in Figure 18. It was found that the dark current for the three types is almost the same. The saturation current increases sharply from type A to type C, and the PD bandwidth increases sharply under high-power operations. The low-power operations bandwidth does not vary much when going from type A to type C PD.

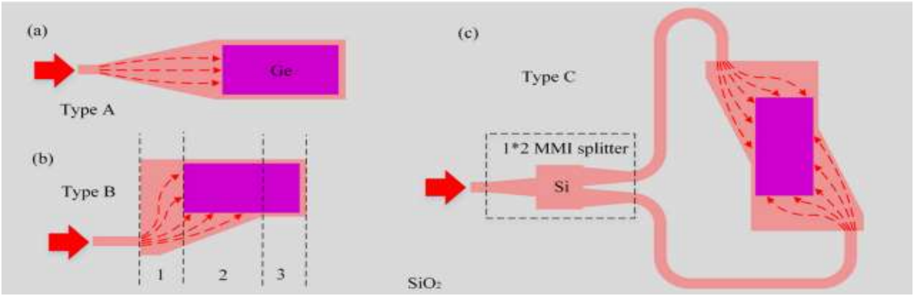

Figure 18. Different optical field manipulation techniques, proposed in [26].

3. Photodiode Integrated Photonic Applications

3.1. MMWave Matching Network Design

The photodiode is a capacitive source, and an inductive matching network must be designed between a photodiode and microwave load. The matching network can be designed directly on the photodiode substrate or a separate substrate where wire or flip-chip bonding connects the matching network to the photodiode. A microwave load is designed with an input impedance of 50Ω; however, this impedance is low, degrading the photodiode sensitivity because of high thermal noise and weaker absorption for the RF photogenerated power. The photodiode matching network uses three approaches to achieve complex conjugate matching between a photodiode and microwave load. First, a matching network is designed between the photodiode and a microwave load. This matching network uses spiral inductors, quarter-wavelength transformers, matching open- or short-circuited shunt CPW stubs, and inductive peaking transmission lines. The inductive peaking transmission line is designed to have a very high characteristic impedance tapered to a low characteristic impedance line to be matched with the microwave load input impedance. The inductive peaking transmission lines are also used to improve the photodiode bandwidth. Second, the antenna input impedance is engineered to achieve an inductive reactance that slowly varies with frequency. The third approach is achieved when a trans-impedance amplifier is used to achieve the impedance matching between a photodiode and microwave load.

The first approach is shown to be used in Figure 19, where resonating mmWave matching networks are presented [36–37]. These resonating matching networks provided a narrow matching bandwidth. It can be seen from Figure 19 that these matching networks are composed of CPW quarter-wavelength transformers and inductive peaking lines. It can also be seen that DC block capacitors are used so that the RF signal is blocked from flowing to the DC bias network and forced to flow into the microwave load.

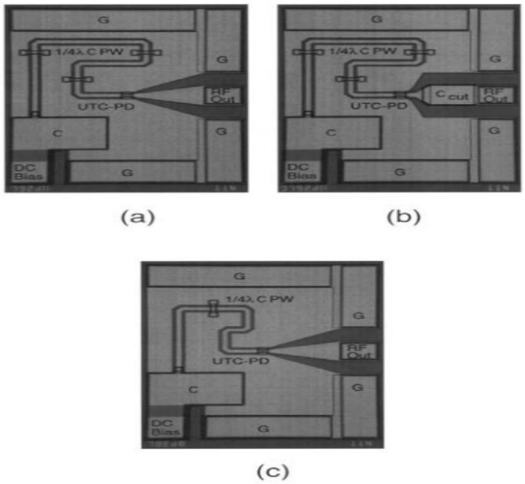

Figure 19. Micrographs of the fabricated photonic microwave generators (PMGs) presented in [36–37].

The second matching approach can be seen in Figure 20 and Figure 21, where the antenna input impedance is achieved to be inductive and compensates for a photodiode's capacitive reactance [38–39]. The antenna geometrical parameters are optimized to achieve the complex conjugate matching between the photodiode and the antenna. The Connected-Array antenna of bowtie elements is designed on an Aluminum Nitride (AlN) substrate [38]. The substrate thickness and dielectric constant of the AlN substrate were optimized to control the antenna input real-part impedance, while the input inductive reactive impedance was achieved using the inductive peaking technique using a coplanar strip line and wire bonds. Furthermore, the antenna metallic dimensions can be optimized to achieve the complex conjugate matching as shown for the proposed Short Asymmetric Inductive Dipole (SAID) antenna in [39]. The proposed photonic antenna in [39] achieved a $1\ GHz$ reconfigurable bandwidth in the frequency range from 26.5 to $40\ GHz$. The antenna input real-part impedance was controlled using the ground and dipole dimensions, as well as the proximity spacing between the dipole and ground. On the other hand, the antenna input inductive imaginary-part impedance was achieved using the two metallic loops around the feeding CPW pads.

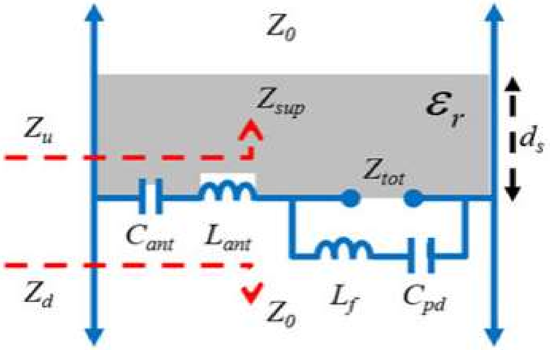

Figure 20. Circuit model for the photonic-integrated connected array antenna in [38].

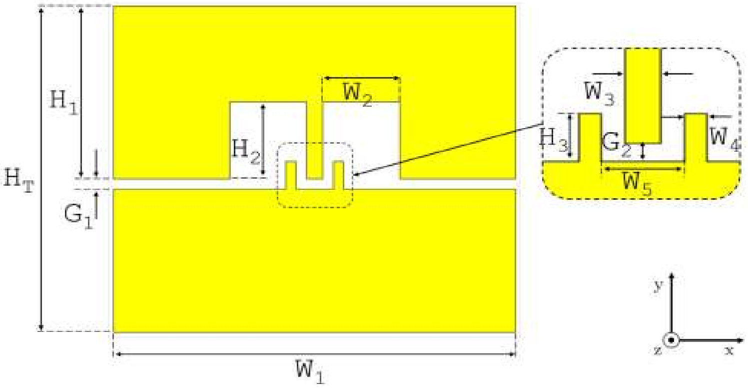

Figure 21. Proposed photonic-integrated SAID antenna in [39].

The third impedance-matching approach is achieved using a trans-impedance amplifier [40] as shown in Figure 22. It can be seen from Figure 22 that three transistors are used to step up the photodiode low output impedance to 50Ω. Unfortunately, this trans-impedance amplifier consumes much power, and achieving a narrow matching bandwidth.

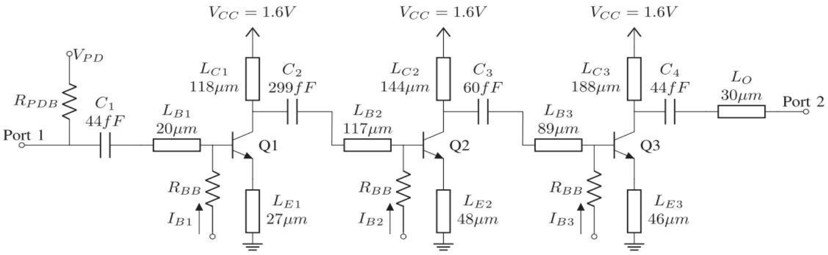

Figure 22. Trans-impedance low-noise amplifier in [40].

Furthermore, the photonic matching network should incorporate a bias-tee such that the photodiode is DC reverse biased, and the RF signal is blocked from flowing to the DC biasing network [41–42]. The DC bias is blocked from flowing into the RF load using an interdigital capacitor as shown in Figure 23 and Figure 24. On the other hand, the RF signal is isolated from flowing into the DC biasing network using a grounded CPW open-circuited shunt stub as shown in Figure 23, or using a band-reject filter as shown in Figure 24. The proposed bias-tee in [41] was designed to operate in the frequency band from 57 to $64\ GHz$, while the bias-tee in [42] operates from 71 to $86\ GHz$.

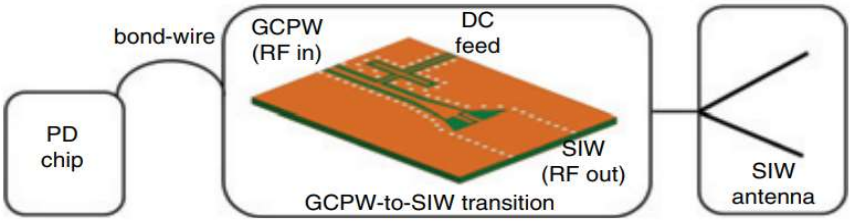

Figure 23. GCPW bias-tee in [41].

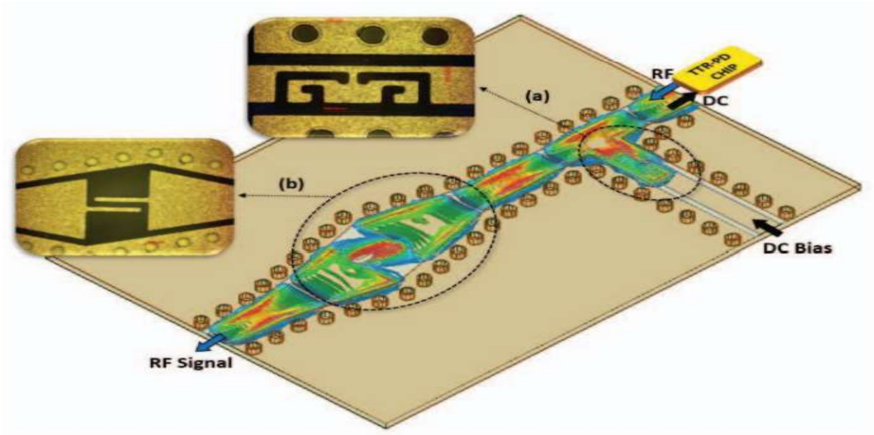

Figure 24. GCPW bias-tee in [42].

3.2. Photodiode Integrated Photonic Emitters

A photonic-integrated quarter-wavelength monopole antenna was designed at 15 GHz on a Silicon chip with a volume of $3 \times 3 \times 0.125\ mm^3$, a gain of $-0.22\ dBi$, and a bandwidth of $800\ MHz$ [43]. The proposed design is shown in Figure 25. The $40\ GHz$ photodiode is connected at the GSG pads shown in Figure 25, where the photodiode is a Ge-on-Si photodiode designed to be operated under low-power conditions.

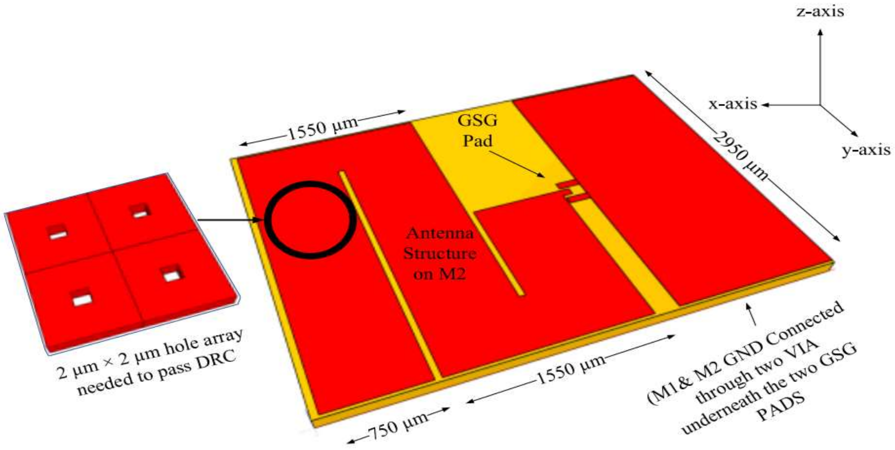

Figure 25. SiPh monopole antenna in [43].

The proposed photonic antenna in [45] was designed in the bandwidth $3.3-3.7\ GHz$ with two matching approaches. The first approach is when the photodiode has its matching network to 50Ω, and the antenna is designed to be well matched to 50Ω, and then the photodiode with its matching network is connected to the antenna. The second approach used antenna input impedance to achieve complex conjugate matching with photodiode output impedance. The proposed photonic antenna in [45] is shown in Figure 26. The output RF current from the photodiode is fed to a patch antenna using a probe feed that goes through an air-filled cavity. The bottom face of the air-filled cavity includes a slot element that divides the cavity into two coupled half-mode cavities, and excites the patch antenna. Therefore, two modes are excited to widen the operating bandwidth.

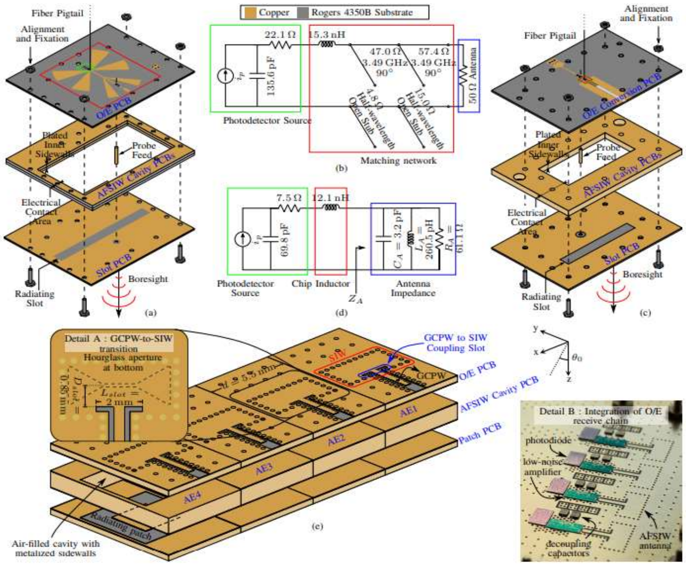

Figure 26. Photonic-integrated slot antenna in [45]. (a) The photonic integrated single-element slot antenna, (b) Equivalent circuit for the single-element slot antenna, (c) The conjugate-matched single-element photonic antenna, (d) Equivalent circuit of the conjugate-matched single-element antenna, and (e) Four elements of a photonic antenna array and an image for the active array.

The proposed photonic antenna design in [48] achieved the complex conjugate impedance matching using the antenna geometry optimization. The proposed photonic antenna in [48] is shown in Figure 27. The antenna is a short asymmetrical inductive dipole achieving a low cross-polarization level, high radiation efficiency, a bandwidth from 25.5 to $31\ GHz$, and a frequency reconfigurability feature when the photodiode reverse bias voltage is varied. Two parallel folded dipoles are used to achieve an impedance transformation and a slowly-varying input impedance with respect to frequency. The antenna theory of operation was explained using the Transmission-Line Mode (TLM) and Radiating Mode (RM). As a result, the characteristic impedance of the Transmission-Line Mode stub and the radius of an equivalent dipole for the proposed antenna can be obtained. Therefore, the antenna input impedance is found considering that the antenna is composed of two parallel monopoles with a lower truncated arm. It was found that the antenna input impedance incorporates a step-up impedance ratio, the impedance of the parallel monopoles, and the coplanar short-circuited stub impedance. Therefore, the real-part of the antenna input impedance was contributed using the TLM, and the imaginary part was contributed using the RM.

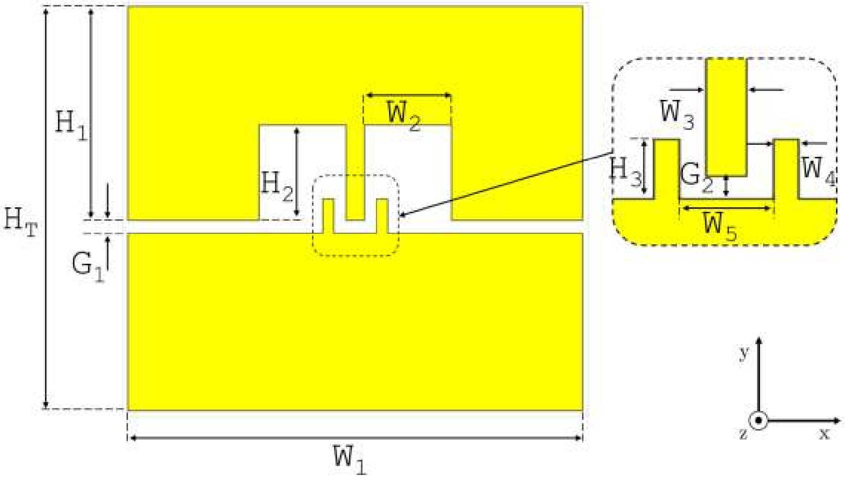

Figure 27. Short asymmetrical inductive dipole antenna in [48].

The work in [46] also integrated an mmWave antenna at 100 GHz with two UTC photodiodes, as shown in Figure 28. The RF signal is fed into the radiating antenna aperture using a coupling slot to block the DC signal from flowing to the radiating antenna. It can be seen from Figure 28(b) that the antenna radiating aperture is made of symmetrical modulated metasurface arrays, which are fed using out of phase RF fields. The metasurface array comprises a capacitive impedance boundary condition sinusoidally modulated along the field propagation direction. The inductive boundary condition is also obtained by using an inductive grounded substrate. Therefore, transverse-magnetic surface waves propagate and radiate because of the periodic modulation.

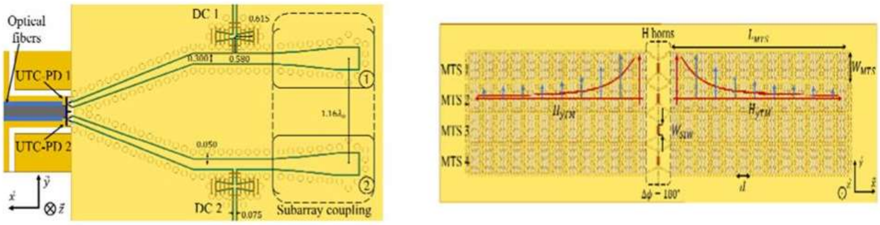

(a) (b)

Figure 28. (a) Top view of the proposed photonic modulated MTS array antenna in [46], and (b) Four modulated MTS subarrays.

The photonic-integrated antenna at $100\ GHz$, as shown in Figure 29, was designed to achieve beam steering [47]. It can be seen that the radiating structure is composed of two stacking patches on a single-mode cavity to achieve a wide operating bandwidth. It can be seen that the RF signal propagates through Substrate Integrated Waveguides (SIWs) to couple to the radiating structure finally. The array grating lobes are reduced using eight elements along the antenna H-plane and two elements along the E-plane. This proposed array is connected to a UTC photodiode, and the beam steering is achieved using optical phase shifters.

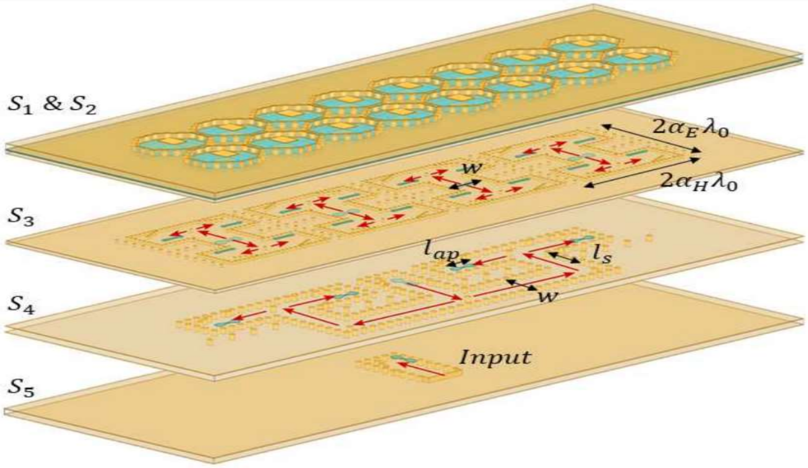

Figure 29. Photonic-integrated subarray antenna in [47].

The photonic-integrated antenna array in [49] was designed to operate in the frequency range from 75 to 86 GHz using a single-element Leaky-Wave antenna with beam steering occurring with respect to the operating frequency. The proposed photonic Leaky-Wave antenna array is shown in Figure 30, where it can be seen that two UTC photodiodes are used to feed the antenna array. The single-element Leaky-Wave antenna comprises four periodic unit-cells connected in series to a microstrip line and a patch element connected at the antenna end. The proposed unit-cell is also presented in Figure 30. It comprises four half-wavelength open-circuited shunt stubs that introduce high-impedance points along the microstrip line. Therefore, the high-impedance points perturb the propagating electromagnetic waves, and signal reflections and losses occur. The single-element Leaky-Wave antenna is optimized to minimize reflections and maximize radiations, and the remaining waves reach to the antenna end and radiate by the patch. This proposed Leaky-Wave antenna array achieved a directivity of $19\ dBi$, and a frequency beam-scanning range of 22^o.

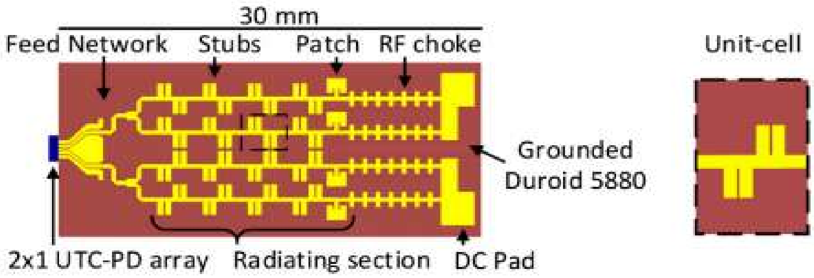

Figure 30. LWA array in [49] and the unit-cell of the radiating section.

The proposed photonic two-element array in [50] used a travelling-wave antenna because of its slowly-varying input impedance versus frequency. The proposed array is shown in Figure 31, where it can be seen that it is composed of two array elements. The proposed antenna array provided a gain of $15.5\ dBi$ in the operating bandwidths from 71 to $76\ GHz$ and from 81 to $86\ GHz$. It was also found that the radiated power from the array is $-6.7\ dBm$ at $70\ GHz$.

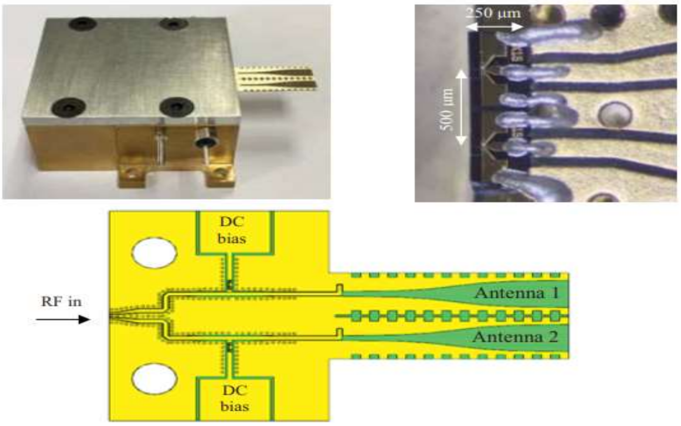

Figure 31. Photonic-integrated antenna array proposed in [50].

The Bowtie antenna was used to achieve a photonic-integrated antenna at $2.5\ THz$ [51], a photonic-integrated Connected Array antenna at 20 GHz [38], and a linear array at 50 GHz [54]. The proposed photonic-integrated Connected Array antenna shown in Figure 32 [38] presented a wideband of operation from 5 to $20\ GHz$ thanks to using the single-element Bowtie antenna. The four photodiodes are Charge-Compensated Modified UTC photodiodes with an output RF power of $23\ dBm$ at $20\ GHz$ for a single photodiode. Flip-chip bonding was used to connect the photodiode to the used Aluminum Nitride (AlN) substrate to increase the photodiode peak RF power. In addition, the coplanar strip output and the wire bonds were used to increase the photodiode's inductive load and improve the impedance matching. Tuning the thickness and dielectric constant of the used AlN substrate improved the impedance matching between the antenna and photodiode. It is worth noting that the small gap between adjacent Bowties works as a capacitive RF short between the array columns. Therefore, a current sheet is achieved, which produces broadside radiation patterns. The proposed photonic Connected Array antenna was capable of steering the beam to $\mp 40^{o}$, and the achieved radiated power from the antenna was more than $15\ dBm$ up to $17\ GHz$.

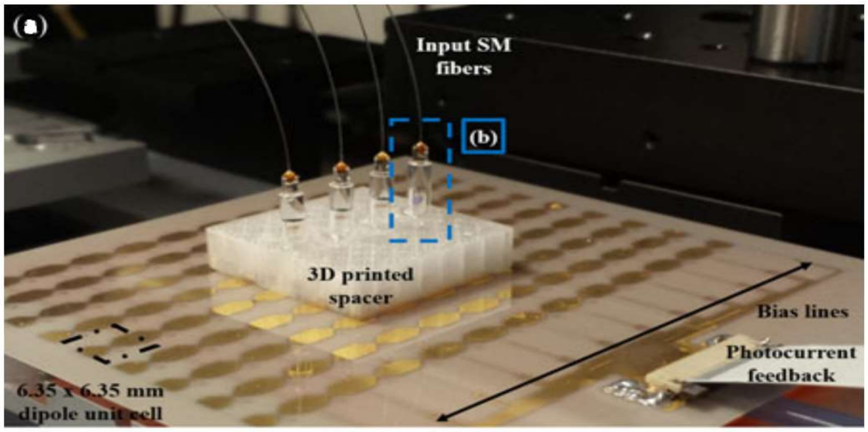

Figure 32. CA antenna in [38] with four single-mode fibers and lens connected to the active antenna elements.

Also, the coplanar-patch antennas at $60\ GHz$ were connected to a photodiode [52–53]. It was found in [53] that the photonic-integrated coplanar-patch, shown in Figure 33, achieved a gain of $4.5\ dBi$ thanks to the inductive peaking matching technique and the used low-loss AlN substrate. While the coplanar-patch antenna, with bandwidth from 56.8 to $66.1\ GHz$, in [52] achieved a gain of $0\ dBi$ because of the used lossy Silicon substrate.

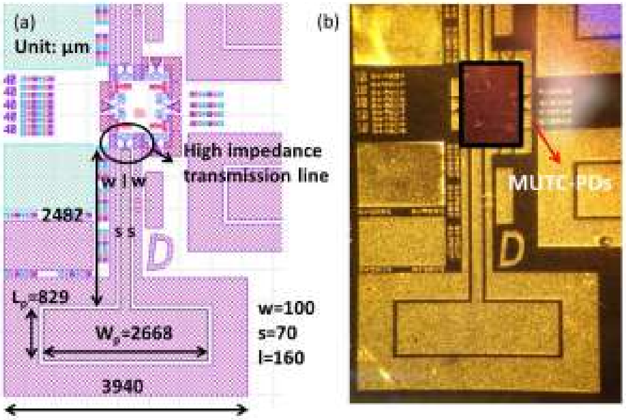

Figure 33. Photonic coplanar patch in [53].

4. Conclusions

The paper has reviewed the recent research on the design of High-Power and High-Speed SiPh Ge-on-Si photodiodes for RoF 5G communications applications. It has been indicated that the HPHS Ge-on-Si PDs are real candidates for the RoF-scheme 5G technology because these PDs have achieved sufficient RF photogenerated powers at mmWave frequencies. The principle and structure for the HPHS SiPh Ge-on-Si photodiodes have been introduced first, and then the equivalent circuit model for the Ge-on-Si photodiode, such that it is possible to obtain the PD S-parameters and bandwidth, has been presented. After that, the PD transit-time and RC-time bandwidths were presented, and the impact of the linear PD array on the overall bandwidth was discussed. After that, the PD photocurrent behavior against the input optical power has been discussed. In addition, the RF photogenerated current mathematics and the optical signal manipulation techniques to improve the saturation current and bandwidth have been discussed. Lastly, the matching network design techniques to match the PD with mmWave antennas have been introduced, and the recent photonic mmWave antenna design has also been presented.

Author Contributions: Conceptualization, S.H.; methodology, software, S.H.; validation, S.H.; formal analysis, S.H.; investigation, S.H.; resources, S.H.; data curation, S.H.; writing—original draft preparation, S.H.; writing—review and editing, S.H., F.F., X.Z., A.K. ; visualization, S.H.; supervision, F.F., X.Z, A.K. ; project administration, F.F., X.Z., A.K. ; funding acquisition, F.F., X.Z., A.K. . All authors have read and agreed to the published version of the manuscript.

Funding: This work was supported by Fonds de Recherche du Québec – Nature et Technologie (FRQNT, Québec).

Institutional Review Board Statement: Not applicable.

Informed Consent Statement: Not applicable.

Data Availability Statement: All data are available within the manuscript.

Conflicts of Interest: The authors declare no conflict of interest.

References

1. "Cisco annual internet Report - Cisco Annual Internet Report (2018–2023) White Paper," *Cisco*, https://www.cisco.com/c/en/us/solutions/collateral/executive-perspectives/annual-internet-report/white-paper-c11-741490.html (accessed Jul. 18, 2023).
2. T. Nagayama, S. Akiba, T. Tomura, and J. Hirokawa, "Photonics-Based MilliMeter-Wave Band Remote Beamforming of Array-Antenna Integrated with Photodiode Using Variable Optical Delay Line and Attenuator," *Journal of Lightwave Technology*, vol. 36, no. 19, pp. 4416–4422, 2018.
3. S. Y. Siew, B. Li, F. Gao, H. Y. Zheng, W. Zhang, P. Guo, S. W. Xie, A. Song, B. Dong, L. W. Luo, C. Li, X. Luo, and G.-Q. Lo, "Review of Silicon Photonics Technology and Platform Development," *Journal of Lightwave Technology*, vol. 39, no. 13, pp. 4374–4389, 2021.
4. A. Beling, X. Xie, and J. C. Campbell, "High-Power, High-Linearity Photodiodes," *Optica*, vol. 3, no. 3, p. 328, 2016. DOI:10.1364/optica.3.000328
5. X. Hu *et al.*, "High-Speed and High-Power Germanium Photodetector with a Lateral Silicon Nitride Waveguide," *Photonics Research*, vol. 9, no. 5, p. 749, 2021. DOI:10.1364/prj.417601
6. M. J. Byrd *et al.*, "Mode-Evolution-Based Coupler for High Saturation Power Ge-on-Si Photodetectors," *Optics Letters*, vol. 42, no. 4, p. 851, 2017. DOI:10.1364/ol.42.000851
7. D. Li *et al.*, "High-Speed and High-Power Ge-on-Si Photodetector with Bilateral Mode-Evolution-Based Coupler," *Photonics*, vol. 10, no. 2, p. 142, 2023. DOI:10.3390/photonics10020142
8. G. Chen, Y. Yu, X. Xiao, and X. Zhang, "High Speed and High Power Polarization Insensitive Germanium Photodetector with Lumped Structure," *Optics Express*, vol. 24, no. 9, p. 10030, 2016. DOI:10.1364/oe.24.010030
9. D. Zhou, G. Chen, S. Fu, Y. Zuo, and Y. Yu, "Germanium Photodetector with Distributed Absorption Regions," *Optics Express*, vol. 28, no. 14, p. 19797, 2020. doi:10.1364/oe.390079
10. 10 X. Luo *et al.*, "Silicon-Based Traveling-Wave Photodetector Array (SI-TWPDA) with Parallel Optical Feeding," *Optics Express*, vol. 22, no. 17, p. 20020, 2014. doi:10.1364/oe.22.020020
11. C.-M. Chang, J. H. Sinsky, P. Dong, G. de Valicourt, and Y.-K. Chen, "High-Power Dual-Fed Traveling Wave Photodetector Circuits in Silicon Photonics," *Optics Express*, vol. 23, no. 17, p. 22857, 2015. doi:10.1364/oe.23.022857
12. T.-C. Tzu *et al.*, "Foundry-Enabled High-Power Photodetectors for Microwave Photonics," *IEEE Journal of Selected Topics in Quantum Electronics*, vol. 25, no. 5, pp. 1–11, 2019. doi:10.1109/jstqe.2019.2911458
13. K. Sun and A. Beling, "High-Speed Photodetectors for Microwave Photonics," *Applied Sciences*, vol. 9, no. 4, p. 623, 2019. DOI:10.3390/app9040623
14. K. Sun *et al.*, "Ge-on-Si Waveguide Photodiode Array for High-Power Applications," *2018 IEEE Photonics Conference (IPC)*, 2018. DOI:10.1109/ipcon.2018.8527107

15. Z. Jiang *et al.*, “High-Power Si-Ge Photodiode Assisted by Doping Regulation,” *Optics Express*, vol. 29, no. 5, p. 7389, 2021. doi:10.1364/oe.417165
16. A. Ramaswamy, M. Piels, N. Nunoya, T. Yin, and J. E. Bowers, “High Power Silicon-Germanium Photodiodes for Microwave Photonic Applications,” *IEEE Transactions on Microwave Theory and Techniques*, vol. 58, no. 11, pp. 3336–3343, 2010. DOI:10.1109/tmtt.2010.2076630
17. J. Michel, J. Liu, and L. C. Kimerling, “High-Performance Ge-on-Si Photodetectors,” *Nature Photonics*, vol. 4, no. 8, pp. 527–534, 2010. DOI:10.1038/nphoton.2010.157
18. M. Piels and J. E. Bowers, “40 GHz Si/Ge Uni-Traveling Carrier Waveguide Photodiode,” *Journal of Lightwave Technology*, vol. 32, no. 20, pp. 3502–3508, 2014. DOI:10.1109/jlt.2014.2310780
19. X. Xie *et al.*, “Heterogeneously Integrated Waveguide-Coupled Photodiodes on SOI with 12 dBm Output Power at 40 GHz,” *Optical Fiber Communication Conference Post Deadline Papers*, 2015. DOI:10.1364/ofc.2015.th5b.7
20. S. A. Srinivasan *et al.*, “27 GHz Silicon-Contacted Waveguide-Coupled Ge/Si Avalanche Photodiode,” *Journal of Lightwave Technology*, vol. 38, no. 11, pp. 3044–3050, 2020. DOI:10.1109/jlt.2020.2986923
21. J.-B. You, H. Kwon, J. Kim, H.-H. Park, and K. Yu, “Photon-Assisted Tunneling for Sub-Bandgap Light Detection in Silicon PN-Doped Waveguides,” *Optics Express*, vol. 25, no. 4, p. 4284, 2017. doi:10.1364/oe.25.004284
22. S. A. Srinivasan *et al.*, “56 Gb/s NRZ O-Band Hybrid BiCMOS-Silicon Photonics Receiver Using Ge/Si Avalanche Photodiode,” *Journal of Lightwave Technology*, vol. 39, no. 5, pp. 1409–1415, 2021. DOI:10.1109/jlt.2020.3038361
23. X. Zeng *et al.*, “Silicon–Germanium Avalanche Photodiodes with Direct Control of Electric Field in Charge Multiplication Region,” *Optica*, vol. 6, no. 6, p. 772, 2019. DOI:10.1364/optica.6.000772
24. K. S. Giboney, M. J. W. Rodwell, and J. E. Bowers, “Traveling-Wave Photodetector Design and Measurements,” *IEEE Journal of Selected Topics in Quantum Electronics*, vol. 2, no. 3, pp. 622–629, 1996. doi:10.1109/2944.571760
25. J. Cui, T. Li, F. Yang, W. Cui, and H. Chen, “The Dual-Injection Ge-on-Si Photodetectors with High Saturation Power by Optimizing Light Field Distribution,” *Optics Communications*, vol. 480, p. 126467, 2021. DOI:10.1016/j.optcom.2020.126467
26. Y. Zuo, Y. Yu, D. Zhou, and X. Zhang, “Integrated High Power Germanium Photodetectors Assisted by Optical Field Manipulation,” *2019 24th OptoElectronics and Communications Conference (OECC) and 2019 International Conference on Photonics in Switching and Computing (PSC)*, 2019. DOI:10.23919/ps.2019.8818034
27. J. M. Senior, Optical Fiber Communications.
28. D. Ahn, L. C. Kimerling, and J. Michel, “Efficient Evanescent Wave Coupling Conditions for Waveguide-Integrated Thin-Film Si/Ge Photodetectors on Silicon-on-Insulator/Germanium-on-Insulator Substrates,” *Journal of Applied Physics*, vol. 110, no. 8, 2011. DOI:10.1063/1.3642943
29. T.-Y. Liow *et al.*, “Silicon Optical Interconnect Device Technologies for 40 Gb/s and Beyond,” *IEEE Journal of Selected Topics in Quantum Electronics*, vol. 19, no. 2, pp. 8200312–8200312, 2013. DOI:10.1109/jstqe.2012.2218580
30. G. Zhou and P. Runge, “Nonlinearities of High-Speed P-I-N Photodiodes and MUTC Photodiodes,” *IEEE Transactions on Microwave Theory and Techniques*, vol. 65, no. 6, pp. 2063–2072, 2017. DOI:10.1109/tmtt.2016.2645152
31. Q. Zhou *et al.*, “High-Power V-Band InGaAs/InP Photodiodes,” *IEEE Photonics Technology Letters*, vol. 25, no. 10, pp. 907–909, 2013. DOI:10.1109/lpt.2013.2253766
32. Q. Li *et al.*, “High-Power Flip-Chip Bonded Photodiode with 110 GHz Bandwidth,” *2015 IEEE Photonics Conference (IPC)*, 2015. DOI:10.1109/ipcon.2015.7323550
33. M. Ali *et al.*, “A Broadband MilliMeter-Wave Photomixing Emitter Array Employing UTC-PD and Planar Antenna,” *2019 44th International Conference on Infrared, Millimeter, and Terahertz Waves (IRMMW-THz)*, 2019. DOI:10.1109/irmmw-thz.2019.8874131
34. J.-M. Wun, C.-H. Lai, N.-W. Chen, J. E. Bowers, and J.-W. Shi, “Flip-Chip Bonding Packaged THz Photodiode with Broadband High-Power Performance,” *IEEE Photonics Technology Letters*, vol. 26, no. 24, pp. 2462–2464, 2014. DOI:10.1109/lpt.2014.2358843
35. J. Xu, X. Zhang, and A. Kishk, “Design of High Speed InGaAs/InP One-Sided Junction Photodiodes with Low Junction Capacitance,” *Optics Communications*, vol. 437, pp. 321–329, Apr. 2019. DOI:10.1016/j.optcom.2018.12.085

36. H. Ito, H. Fushimi, Y. Muramoto, T. Furuta, and T. Ishibashi, "High-Power Photonic Microwave Generation at K- and Ku-Bands Using a Uni-Traveling-Carrier Photodiode," *2001 IEEE MTT-S International Microwave Symposium Digest (Cat. No.01CH37157)*.
37. H. Ito, A. Hirata, T. Minotani, Y. Hirota, T. Ishibashi, A. Sasaki, and T. Nagatsuma, "High-Power Photonic MilliMetre Wave Generation at 100 GHz Using Matching-Circuit-Integrated Uni-Travelling-Carrier Photodiodes," *IEE Proceedings - Optoelectronics*, vol. 150, no. 2, pp. 138–142, 2003.
38. M. R. Konkol, D. D. Ross, S. Shi, C. E. Harrity, A. A. Wright, C. A. Schuetz, and D. W. Prather, "High-Power Photodiode-Integrated-Connected Array Antenna," *Journal of Lightwave Technology*, vol. 35, no. 10, pp. 2010–2016, 2017.
39. S. Vega et al., "Compact Optically-Fed Antennas with Reconfigurable Frequency Operation in the Ka Band," 2023. DOI:10.2139/ssrn.4497242
40. N. Singh et al., "60 GHz Resonant Photoreceiver with an Integrated SiGe HBT Amplifier for Analog Radio-over-Fiber Links," *2020 European Conference on Optical Communications (ECOC)*, 2020. DOI:10.1109/ecoc48923.2020.9333334
41. I. Flammia, B. Khani, S. Arafat, and A. Stöhr, "60 GHz Grounded-Coplanar-Waveguide-to-Substrate-Integrated-Waveguide Transition for RoF Transmitters," *Electronics Letters*, vol. 50, no. 1, pp. 34–35, 2014. DOI:10.1049/el.2013.3533
42. B. Khani *et al.*, "Compact E-Band (71–86 GHz) Bias-Tee Module for External Biasing of Millimeter Wave Photodiodes," *2015 International Topical Meeting on Microwave Photonics (MWP)*, 2015. DOI:10.1109/mwp.2015.7356673
43. B. Radi, A. S. Dhillon, and O. Liboiron-Ladouceur, "Demonstration of Inter-Chip RF Data Transmission Using on-Chip Antennas in Silicon Photonics," *IEEE Photonics Technology Letters*, vol. 32, no. 11, pp. 659–662, 2020.
44. P. Burasa, T. Djerafi, and K. Wu, "A 28 GHz and 60 GHz Dual-Band on-Chip Antenna for 5G-Compatible IoT-Served Sensors in Standard CMOS Process," *IEEE Transactions on Antennas and Propagation*, vol. 69, no. 5, pp. 2940–2945, 2021.
45. O. Caytan *et al.*, "Co-Design Strategies for AFSIW-Based Remote Antenna Units for RFoF," *2023 17th European Conference on Antennas and Propagation (EuCAP)*, 2023. DOI:10.23919/eucap57121.2023.10133123
46. J. Taillieu, R. Sauleau, M. Alouini, and D. G. Ovejero, "Modulated Metasurface Array for Photonic Beam Steering at W Band," *2023 17th European Conference on Antennas and Propagation (EuCAP)*, 2023. DOI:10.23919/eucap57121.2023.10133650
47. J. Taillieu, R. Sauleau, M. Alouini, and D. Gonzalez-Ovejero, "Cavity-Backed Broadband Microstrip Antenna Array for Photonic Beam Steering at W Band," *2022 16th European Conference on Antennas and Propagation (EuCAP)*, 2022. DOI:10.23919/eucap53622.2022.9769419
48. C. Ballesteros, S. Vega, M. C. Santos, and L. Jofre-Roca, "Short Asymmetrical Inductive Dipole Antenna for Direct Matching to High-Q Chips," *IEEE Antennas and Wireless Propagation Letters*, vol. 22, no. 1, pp. 149–153, 2023. DOI:10.1109/lawp.2022.3204841
49. Á. J. Pascual-Gracia, M. Ali, G. Carpintero Del Barrio, F. Ferrero, L. Brochier, R. Sauleau, L. E. García-Muñoz, and D. González-Ovejero, "A Photonically-Excited Leaky-Wave Antenna Array at E-Band for 1-D Beam Steering," *Applied Sciences*, vol. 10, no. 10, p. 3474, 2020.
50. M. Ali, R. C. Guzman, F. van Dijk, L. E. Garcia-Munoz, and G. Carpintero, "An Antenna-Integrated UTC-PD Based Photonic Emitter Array," *2019 International Topical Meeting on Microwave Photonics (MWP)*, 2019.
51. C. C. Renaud, M. Natrella, C. Graham, J. Seddon, F. Van Dijk, and A. J. Seeds, "Antenna Integrated THz Uni-Traveling Carrier Photodiodes," *IEEE Journal of Selected Topics in Quantum Electronics*, vol. 24, no. 2, pp. 1–11, 2018.
52. 52. K. Furuya, S. Akiba, J. Hirokawa, and M. Ando, "60 GHz-Band Compact Photonic Antenna Module with Integrated Photodiode," *IEEE International Symposium on Antennas and Propagation (ISAP)*, 2016.
53. K. Li *et al.*, "High-Power Photodiode Integrated with Coplanar Patch Antenna for 60-GHz Applications," *IEEE Photonics Technology Letters*, vol. 27, no. 6, pp. 650–653, 2015. DOI:10.1109/lpt.2015.2389652
54. Jankowski, A., van Dijk, F., Larrue, A., Garcia, M., Gomez, C., and Pommereau, F., "Antenna-Integrated Photodiode Array with Single Optical Input," *2020 International Topical Meeting on Microwave Photonics (MWP)*. https://doi.org/10.23919/mwp48676.2020.9314594